Focused Monostatic and Bistatic Range Doppler Imaging of Rotating Targets with a Coherent Pulse Radar

Michael Kleintz

DLR - Institute for Radio Frequency Techniques
D-8031 Oberpfaffenhofen (Germany)

INTRODUCTION

To discuss imaging properties, a target is assumed to be composed of a great number of scattering points located on its surface. The field strenght at the receiving antenna is the coherent sum of these point echoes; the motion of the scattering points due to the rotation of the target. The radar echo from the target is measured by a coherent short-pulse radar working in a quasi-cw mode and depends on the adjusted center of the range-gate delay time. It contains down range and cross range information in amplitude and phase via the observed range-gated Doppler spectrum.

The radar image of the visible parts of the target will be processed from the coherent sum of point-responses from all point scatterers, whereby the resolution is obtained in two of three spatial coordinates: the complex distribution of reflectivity function is down range (slant range or delay time) and cross range (doppler shift) is a horinzontal projection of the 3D-distribution. Down range and cross range are interpreted as far-field variables - disturbing near-field terms of slant range as well as doppler effect of higher order may by eliminated by focusing - both for monostatic and bistatic geometry and will be related by a linear transform (central extension and rotation) to the cartesian coordinates of the target turntable. By this means it is possible to define a system of coordinates generally valid for monostatic and bistatic geometry (e.g. appropriate to point by point correlation for polarimetric studies). In the case of unfocused imaging the physical effects caused by the terms of Taylor's series expansion of slant range dependent on location and time will be shown: the distortion of central perspective is caused by the time-independent slant-range terms of second and higher order in conjuction with the near-field doppler terms of first and higher order. The blurring of cross-range resolution is produced by the variation terms doppler shift in time domain. The blurring of down-range resolution is caused by range-migration due to the real motion of the scattering centers. Focusing compensates phase shift by correlation with the inverse doppler-phase-function (first and higher doppler terms) as well as the phase of the range-migration. The latter effect corresponds to a phase distortion in the Fourier-space and will be compensated after Fourier transform (from the down-range domain to the k-domain) by correlation with the inverse phase function due to range-migration. The two-dimensional inverse Fourier transform back to the local domain will give the focused radar image. It should be mentioned that this inverse Fourier transform cannot be computed by the usual FFT-routines, because the spectra depend on the location of the actual point to be processed.

Radar images of point scatterers from simulated and measured data will be compared with the theoretically calculated point-spread-functions.

Finally a special example for failure of the point-scatterer imaging is shown: the backscatter from a right elliptical cylinder is marked by migration of the speculare point which does not conform to the geometrical motion. Imaging, unfocused as well as focused (in the upper sense), will not allow satisfactory results in resolution. The locus of the specular point versus the angle of rotation can be defined theoretically and used for a special focusing algorithm.

1. THE RADAR ECHO AND ITS INFORMATION CONTENT

1.1 The coherent short-pulse radar equipment

The transmitter oscillator is driven by a phaselock-loop controlled synthesize. A pulse generator in connection with a pulse shaper keys (adjustable pulse lenght τ_T) the amplitude of the output stage of the transmitter system, and will be radiated by the transmitter antenna. The radar echo is received by a separate antenna also with adjustable

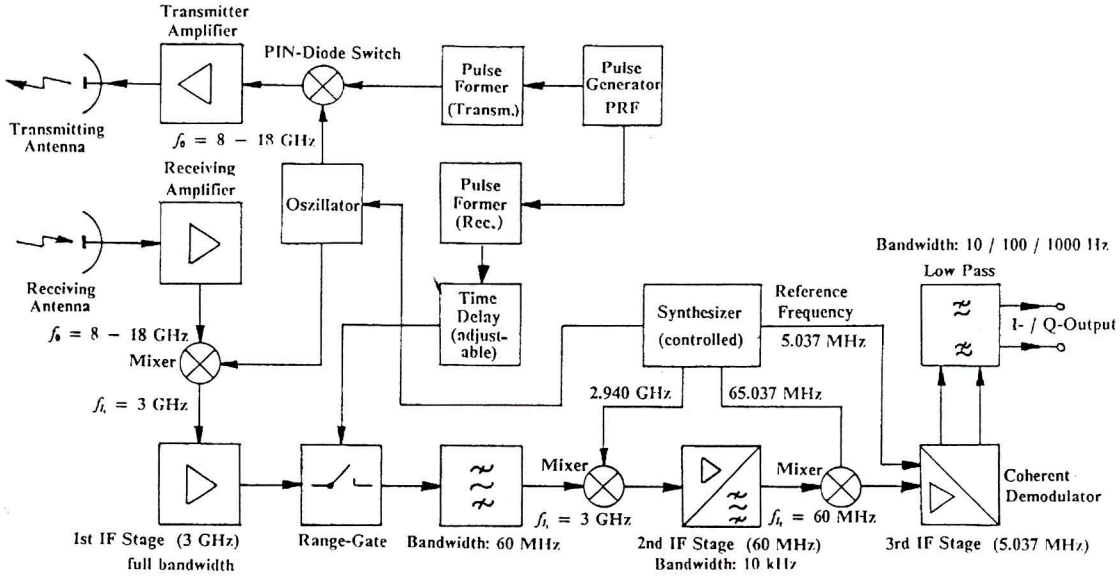

Fig. 1 - Block Diagram o the coherent short-pulse radar.

polarization. The front end amplifier is followed by a mixer with a first intermediate frequency of 3 GHz; the output of this amplifier has full bandwidth for range-gating the pulse echo. Within the next states (2nd and 3rd IF amplifiers at 60 MHz and 5.037 MHz) the signal bandwidth is limited stepwise (output band-width = 1000/100/10 Hz). Thereby, the pulse radar works in a quasi-cw-mode like a sampled system. The receiver system has a coherent output (I and Q) in the base-band. The bandwidht of the receiver output must be sufficiently large to let pass the highest doppler shifted radar echoes. Fig. 1 shows the block diagram the block diagram of the coherent short-pulse radar, tab. 1 the system parameters.

1.2 The received signal

The cw-radar return (definitions see (Kleintz, 1992)) is described by an integral over an area (A) of the infinitesimal contributions of the reflectivity $s\,(x,y)$. These are weighted by the complex phase factor $\exp(-jk\,R\,(x,y,t))$ due to the lenght $R\,(x,y,t)$ of the propagation path, dependent on location and time because of the target rotation. The transmission factor of the radar path is called g_0 and contains antenna patterns, free-space propagation losses etc. If the target is illuminated homogeneously, this factor can be taken ahead of the integral. A time delay filter (range gate) y_R separates the range echo into contributions of the lenght δR in the neighbourhood

Table 1. Technical data of the coherent short-pulse-radar.

System Parameters	
Frequency	linearly swept or fixed, X-/Ku-Band 8 - 18 GHz
Polarization	linear (HH, VV, VH, HV) or circular
Range	50 - 100 m (here: 131 m)
Transmitter	
Output Amplifier	Travelling Wave Tube, 40 W Peak Power
Pulsewidht	0.8 ns $\le \tau_T \le$ 1000*ns*
PRF	1*kHz* $\le f_{PRF} \le$ 1000*kHz*
Receiver	
Type	Phaselock-Loop Controlled Superheterodyne
Range Gate	0.8*ns* $\le \tau_R \le$ 1000*ns*
Video Output	Amplitude (logarithmic), I/Q (linear)
Video Bandwith	variable, 10*Hz* $\le \Delta f \le$ 20*kHz*
Range	0*ns* $\le \tau \le$ 9999*ns* (continuously or-stepwise)
Antennas	
Type	70 cm Parabol. Refl. (XMTR/RCVR separated)
3-dB-Beamwidth	both 2.6° at f_0 = 11.43*GHz*
Turnable	2-Axes (Elev. over Azimuth), by Remote-Control
Angular Range	± 4 θ (Azimuth), - 10° up to 90° (Elevation)
Precision	± 0.01^0

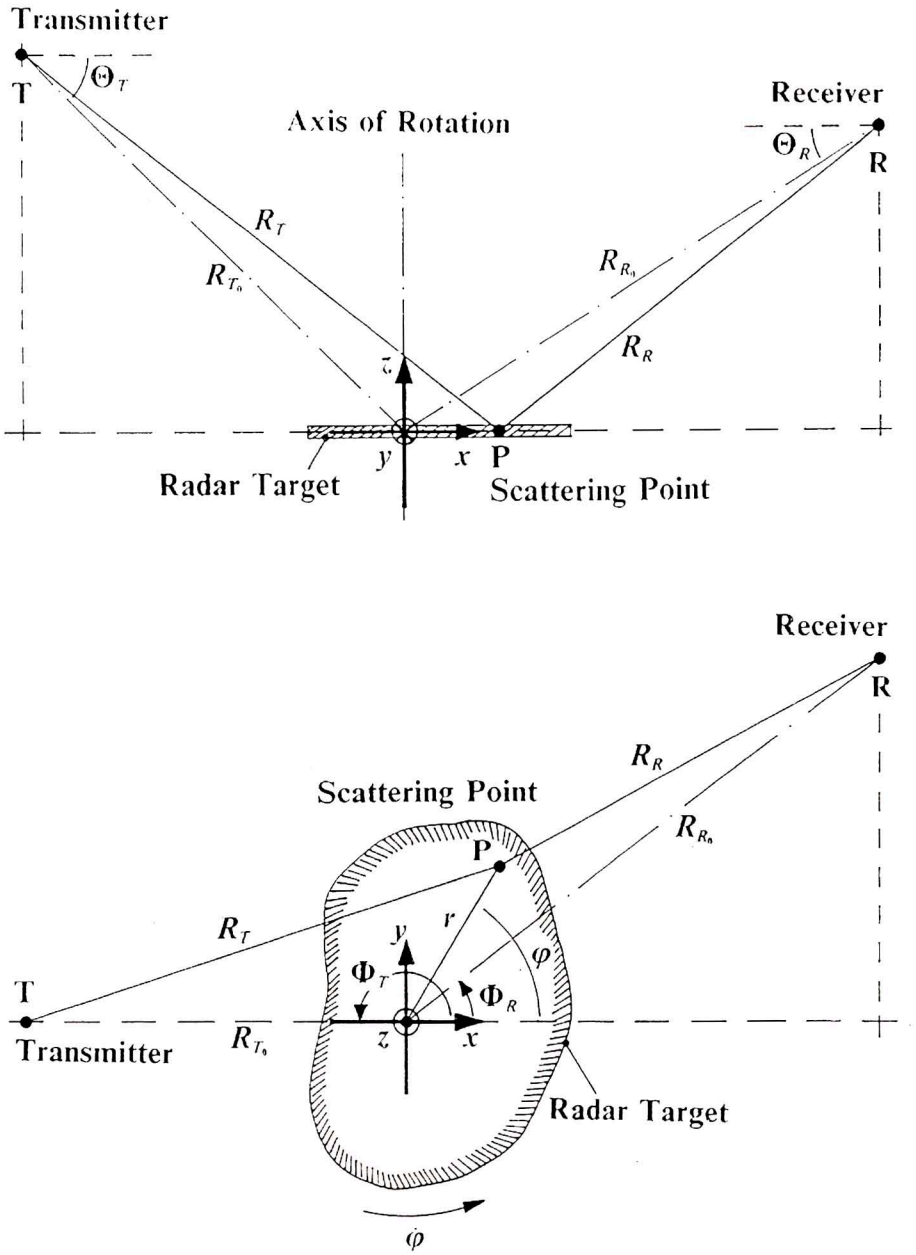

Fig. 2 - Bistatic geometry.

of the center delay $\overline{R}$. The signal equation for the radar echo from a moving target is in general

$$S(\overline{R},t)=g_0 \iint_{(\Lambda)} s\,(x,y)\, e^{-jkR\,(x,y,t)}\, y_R\,[\,R\,(x,y,t)-\overline{R}\,;\,\delta R\,]\,dx\,dy \qquad (1.2\text{-}1)$$

1.3 Geometry and information content of the bistatic measurements

For bistatic geometry the term $R\,(x,y,t)$ will be

$$R(x,y,t)=\left(R_{T_0}^2+2R_{T_0}\cos\Theta_T\,(x\cos\dot{\varphi}t-y\sin\dot{\varphi}t)+x^2+y^2\right)^{1/2}+$$

$$+\left(+R_{R_0}^2-2R_{R_0}\cos\Theta_R\,(x\cos(\dot{\varphi}t-\Phi_R)-y\sin(\dot{\varphi}t-\Phi_R)\,]+x^2+y^2\right)^{1/2} \qquad (1.3\text{-}1)$$

This expression is to be expanded to a Taylor's series in terms of x, y and t, whereby $\dot{\varphi}t$ denotes the instantaneous rotation angle of the turntable. The Taylor's expansion in time and location can be written as a sum of several terms: a constant term contains the main axes $R_0 = R_{T_0} + R_{R_0}$, a time constant linear term in (x, y) denotes the far-field

limit of down range R_L (x,y) related to the axis of rotation, and a variation term due to the rotation of the target and to near-field effects $\Delta R\,(x,y,t)$

$$R\,(x,y,t) = R_0 + R_L\,(x,y) + \Delta R\,(x,y,t)\ . \qquad (1.3\text{-}2)$$

The phase factor dependent on R_Q in first order is the far-field doppler shift given by

$$k\dot{\varphi}t \cdot R_Q = -\,\omega_0 \frac{\partial\,(R_L)}{\partial\,t}\,t = \omega_d\,t = -\,k_Q\,R_Q$$

The term k_Q is the spatial frequency in the axis of cross range, the term $k_Q\,R_Q$ is a Fourier-term. Thus, the variation term will be the sum of this Fourier-term and the remainder $\Delta R'\,(x,y,t)$, which describes doppler distortions due to near-field effects and higher order in the time (or k_Q) domain

$$\Delta R\,(x,y,k_Q) = -\,\frac{k_Q}{k}\,R_Q\,(x,y) + \Delta R'\,(x,y,k_Q)\ . \qquad (1.3\text{-}4)$$

R_L has been mentioned as the far-field down range term related to the axis of rotation; R_Q denotes the cross range term defined also as a far-field limit of ΔR. These variables result from the limit of infinite distances R_{T_0} and R_{R_0}, and define a vector with perpendicular components

$$\vec{R} = \begin{pmatrix} R_L \\ R_Q \end{pmatrix} = \begin{pmatrix} \cos\Theta_T - \cos\Theta_R \cos\Phi_R & -\cos\Theta_R \sin\Phi_R \\ \cos\Theta_R \sin\Phi_R & \cos\Theta_T - \cos\Theta_R \cos\Phi_R \end{pmatrix} \cdot \begin{pmatrix} x \\ y \end{pmatrix}\ . \qquad (1.3\text{-}5)$$

The inversion of this system of linear equations (1.3-5) is possible, if the determinant of the transformation matrix does not equal zero. The geometric position of a scattering point in the (x,y) - plane is given by the relationship

$$\vec{r} = \begin{pmatrix} x \\ y \end{pmatrix} = \frac{1}{\alpha} \cdot \left(M_N^{-1} \cdot \vec{R} \right)\ ,$$

which is a central extension combined with a rotation, whereby the inverse extension factor is

$$\alpha = \sqrt{\cos^2\Theta_T + \cos^2\Theta_R - 2\cos\Theta_T \cos\Theta_R \cos\Phi_R} \qquad (1.3\text{-}6a)$$

and the normalized rotation matrix

$$M_N^{-1} = \frac{1}{\alpha} \begin{pmatrix} \cos\Theta_T - \cos\Theta_R \cos\Phi_R & \cos\Theta_R \sin\Phi_R \\ -\cos\Theta_R \sin\Phi_R & \cos\Theta_T - \cos\Theta_R \cos\Phi_R \end{pmatrix}\ . \qquad (1.3\text{-}6b)$$

With $k_Q = -\,k\,\dot{\varphi}t$ and $dx\,dy = dR_L\,dR_Q/\alpha^2$ eq. (1.2-1) can be written as a partial spectrum dependent on locus (in equidistant steps of the raster $\delta R_0 : \bar{R}_L = \mu \cdot \delta R_0$ and spatial frequency in cross range direction k_Q

$$S\left(\bar{R}_L\,,\,k_Q\right) = \frac{g_0\,e^{-\,jkR_0}}{\alpha^2} \iint\limits_{(A)} s\,(R_L\,,R_Q)\,e^{-\,jk\Delta R'\,(R_L,R_Q;k_Q)}\,\cdot\, y_R\Big[\,R_L - \left(\bar{R}_L - \Delta R\left(R_L\,,R_Q\,;k_Q\right)\right);\,\delta R\,\Big]\,dR_L \cdot e^{-\,jk_Q R_Q} dR_Q \qquad (1.3\text{-}7)$$

The down range resolution is executed by hardware and is described by a convolution with the range gate function γ_R. The boundaries of integration may be extended to infinity, because the reflectivity $s\,(x,y)$ of the target is limited in its local size.

2. SIMULATIONS OF POINT SCATTERERS

2.1 Methods of imaging

The first order evaluation of data is a simple windowed Fourier-transform in the cross range axis (Q) for each step of $\bar{R}_L$. The window function is assumed for an analytical approach e.g. to be Gaussian with an effective width of $\Delta k_Q = k\Delta\varphi$ ($\Delta\varphi$ is the angle interval of data processing). The exact point-spread-function is rather complicated (see (Kleintz, 1986), eq. (3.3.-2)). Therefore we shall reference here only the results for some special cases:
For monostatic geometry ($\Phi_R = \Phi_T = \pi$, $\Theta_R = \Theta_T = \Theta_0$ and $R_{T_0} = R_{R_0} = R_0$) we get a resolution in the neighbourhood of the down range axis, whereby r denotes the distance between the scattering point P and the axis of rotation, given by

$$\Delta_{x\parallel} = \frac{\delta R}{2} \text{ and } \Delta y_{\parallel} = \frac{\lambda}{2\Delta\varphi}\sqrt{1+\alpha_Q^2}\ ,\ \text{with } \alpha_Q = \frac{r\Delta\varphi}{\lambda/2\Delta\varphi}\ . \qquad (2.1\text{-}1a,b)$$

In the neighbourhood of the cross range axis we get

$$\Delta x_{=} = \frac{\delta R}{2}\sqrt{1+\alpha_L^2} \text{ and } \Delta y_{=} = \frac{\lambda}{2\Delta\varphi}\sqrt{1+\alpha_L^2}\ ,$$

$$\text{with } \alpha_L = \frac{r\Delta\varphi}{\delta R/2}\ . \qquad (2.1\text{-}1c,d)$$

A higher order evaluation of data must compensate the doppler distortions $k\Delta R'\,(R_L\,,R_Q\,;k_Q)$ and the range migration $\Delta R\,(R_L\,,R_Q\,;k_Q)$. The first step is the Fourier transform from the down range domain $\bar{R}_L$ to the spatial frequency domain k_L, whereby shifts in the local domain correspond to a proportional phase shift. The full spectrum in the space frequency domain depends on the location in R_L and R_Q; therefore, a two-dimensional correlation with the inverse phase-error funcion must be carried out point by point followed by a (windowed) two-dimensional inverse Fourier transform. Because of the locally dependent spectra, the use of FFT algorithms is not possible. The

resolution for monostatic geometry will be for all points of the (x,y)-plane isotropically

$$\Delta x = \frac{\delta R}{2}, \text{ and } \Delta y = \frac{\lambda}{2\Delta\varphi} . \qquad (2.1\text{-}2a,b)$$

Further details about the resolution for monostatic imaging are given in (Kleintz, 1986) and (Kleintz, 1992).

2.2 Monostatic simulations of point scatterers

The scenario is a simulated arrangement of point scatterers, which are reflecting isotropically with the same amplitude. One scatterer is located in the center of rotation, always four scatterers in a radial distance of 1.5 m in down range, cross range and diagonal directions. All following radar images have a dynamic range of 30 dB normalized to the maximum.

The number of samples in range is 128, in azimuth 256 (the effective number is 128 because of Hamming-windowing). With an angular increment of $\delta\varphi = 0.03^0$ we get an effective angular interval of $\Delta\varphi = 3.84^0$ corresponding to a cross range resolution of $\Delta y = 0.15m$ at a wavelength of $\lambda = 2cm$ (= down range resolution Δx). The spatial resolution is in agreement with the raster δR_0 in down and cross range. The sizes of the images are 94 x 94 pixels (figs. 3-9, fig. 17) and 32 x 32 pixels (figs. 10-15) according to object diameters of 14.1 m and 4.8 m for monostatic geometry at $\Theta_0 = 0^0$.

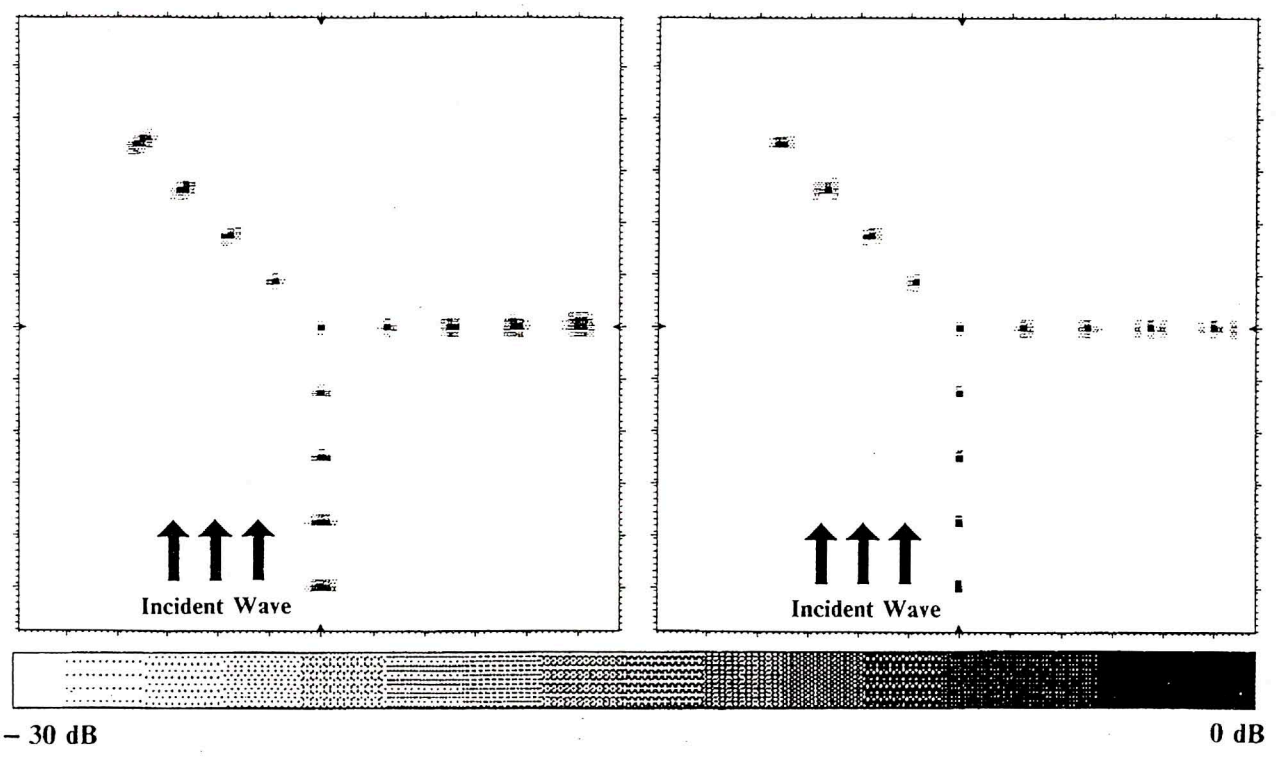

Fig. 3 - Simulated point scatterers (monostatic geometry) unfocused (l) focused (r)
$\delta R = 30cm$, $\lambda/\Delta\varphi = 30cm$, $\lambda = 2cm$, $\Theta_0 = 0^0$, $\alpha = 2.0$.

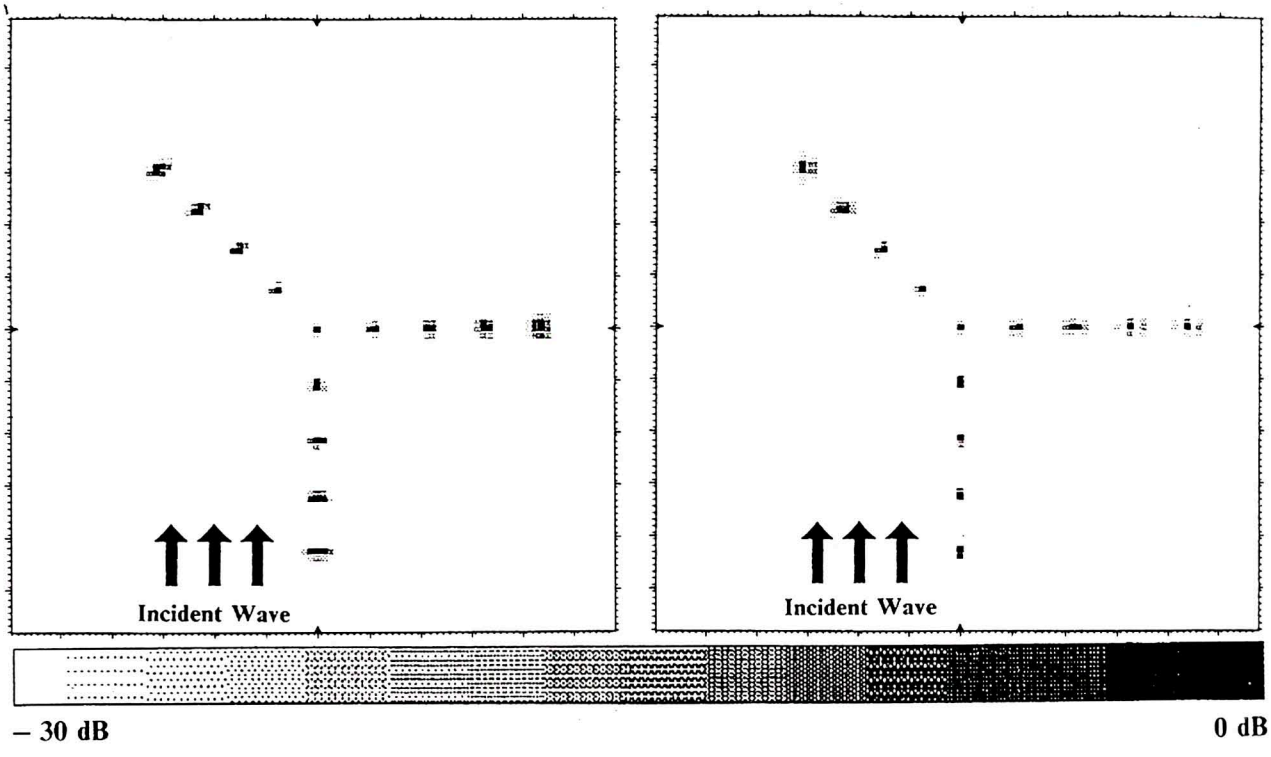

Fig. 4 - Simulated point scatterers (monostatic geometry) unfocused (1) focused (r)
$\delta R = 30cm$, $\lambda/\Delta\varphi = 30cm$, $\lambda = 2cm$, $\Theta_0 = 30^0$, $\alpha = \sqrt{3}$.

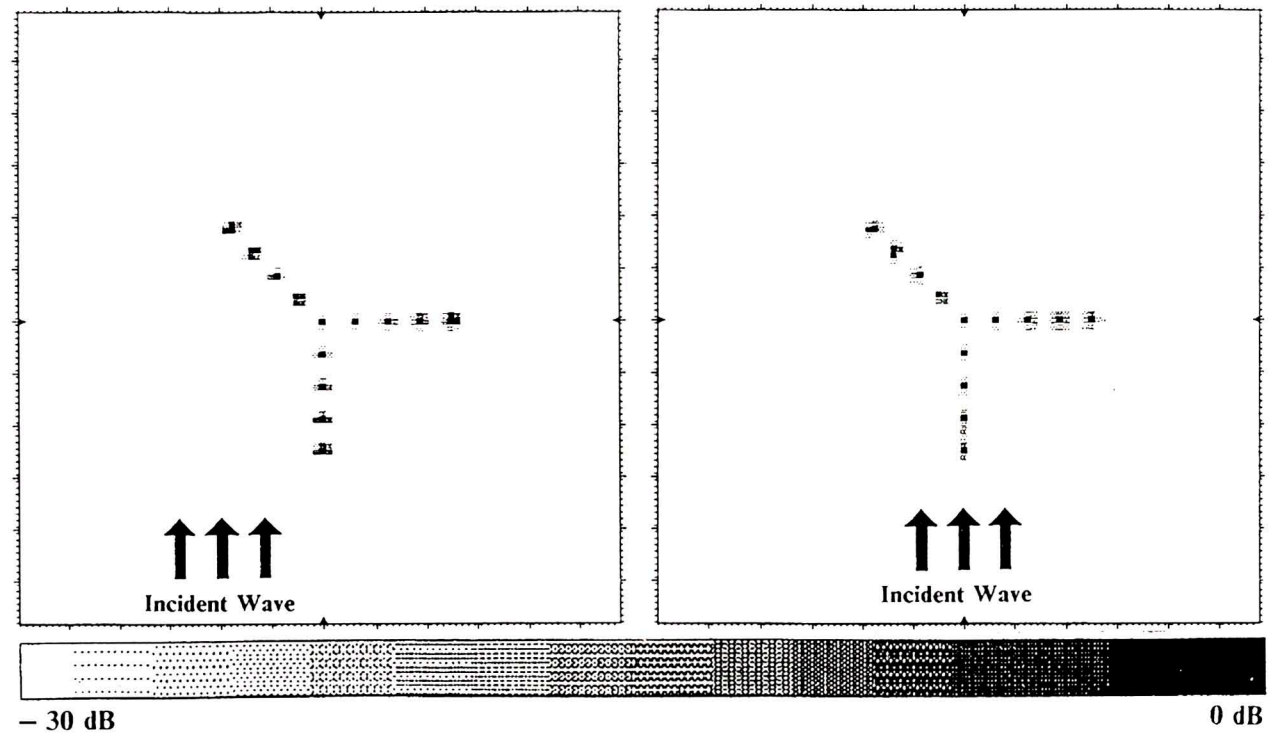

Fig. 5 - Simulated point scatterers (monostatic geometry) unfocused (1) focused (r)
$\delta R = 30cm$, $\lambda/\Delta\varphi = 30cm$, $\lambda = 2cm$, $\Theta_0 = 60^0$, $\alpha = 1.0$.

In the down range axis the resolution becomes optimal; in the cross range axis some sidelobe effects are visible (s.l. ratio about 17 dB), but also with a clear effect of focusing. Fig. 4 shows the same scenario at a depression angle $\Theta_0 = 30°$. At a depression angle of $\Theta_0 = 60°$ (fig. 5) $\alpha = 1.0$ has decreased to the half size of fig. 3.

2.3 Bistatic simulations of point scatterers

The scenario of bistatic simulation is the same as the monostatic scenario. The bistatic angle is given by

$$\Phi_{bs} = \arctan\left(\frac{\cos\Theta_R \sin\Phi_R}{\cos\Theta_T - \cos\Theta_R \cos\Phi_R}\right) \xrightarrow{\Theta_T = \Theta_R} \frac{\Phi_R + \pi}{2}. \quad (2.3\text{-}1)$$

Fig. 6 is valid for $\Phi_R = 120^0$ or $\Phi_{bs} = 150^0$; the extension factor will then be $\alpha = \sqrt{3}$. Fig. 7 is valid for $\Phi_R = 90^0$ or $\Phi_{bs} = 135^0$; the extension factor will then be $\alpha = \sqrt{2}$. Fig. 8 is valid for $\Phi_R = 60^0$ or $\Phi_{bs} = 120^0$; the extension factor will then be $\alpha = \sqrt{1}$. Finally Fig. 9 gives an example in the vicinity of forward scattering (i.e. the singularity of the linear equations (2.3-6,7) with $\Phi_R = 5^0$ or $\Phi_{bs} = 92.5^0$ and an extension factor $\alpha = 0.087$. In this case the radar image shrinks to a small cluster, and the details are hardly discernible. The azimuth angle should not be much less than 90° in order to get acceptable local resolution.

3 MONOSTATIC MEASUREMENTS AND LIMITATIONS OF THE POINT SCATTERER MODEL

3.1 Scenario with point scatterers

The following measurements have been taken with a scenario of biconical reflectors in order to validate the model of point scatterers: One scenario uses each two reflectors with diameters of 20 cm in the center of rotation and (as shown in figs. 11 and 15) in a distance of 120 cm from the central point, and two with diameters of 10 cm in a radial distance of $150 \pm 15cm$ from the central point. The other scenario uses the 20 cm reflectors in the same position; but the smaller ones are now placed in a radius of each 1.50 m in an azimuthal distance of $\pm 15cm$ (see figs. 12 and 14). The scenario of simulation combines the scenarios of measurement (see figs. 10 and 13). The resolution of unfocused imaging depends on the product of the

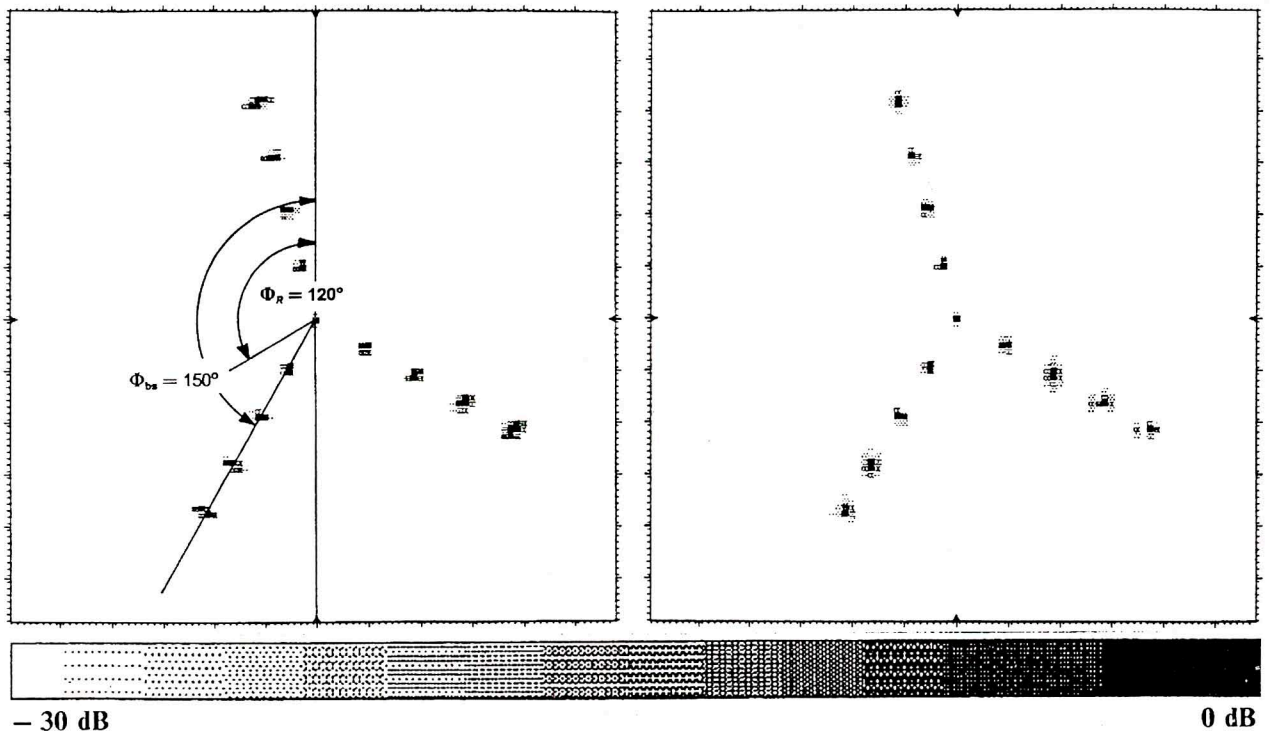

Fig. 6 - Simulated point scatterers (monostatic geometry) unfocused (1) focused (r)
$\delta R = 30cm$, $\lambda/\Delta\varphi = 30cm$, $\lambda = 2cm$, $\Theta_T = \Theta_R = 0^0$, $\Theta_R = 120^0$

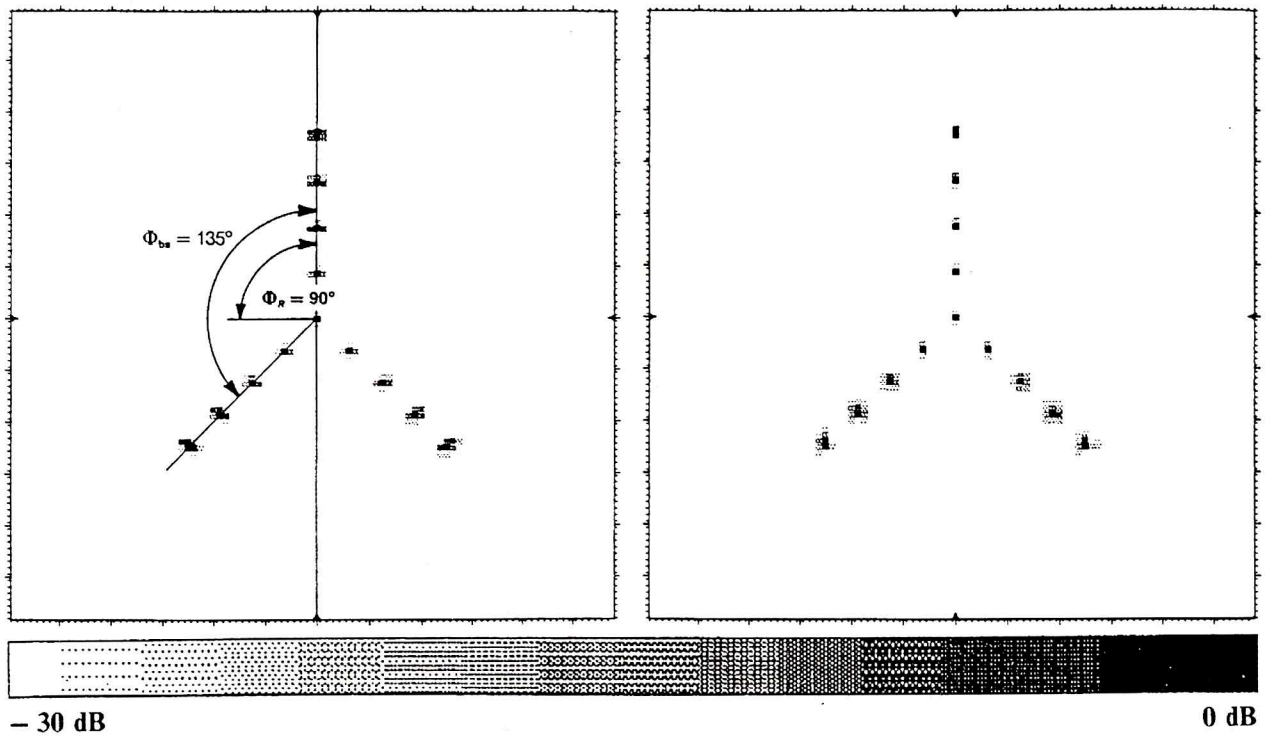

Fig. 7 - Simulated point scatterers (bistatic geometry) unfocused (1) focused (r)
$\delta R = 30cm$, $\lambda/\Delta\varphi = 30cm$, $\lambda = 2cm$, $\Theta_T = \Theta_R = 0^0$, $\Theta_R = 60^0$.

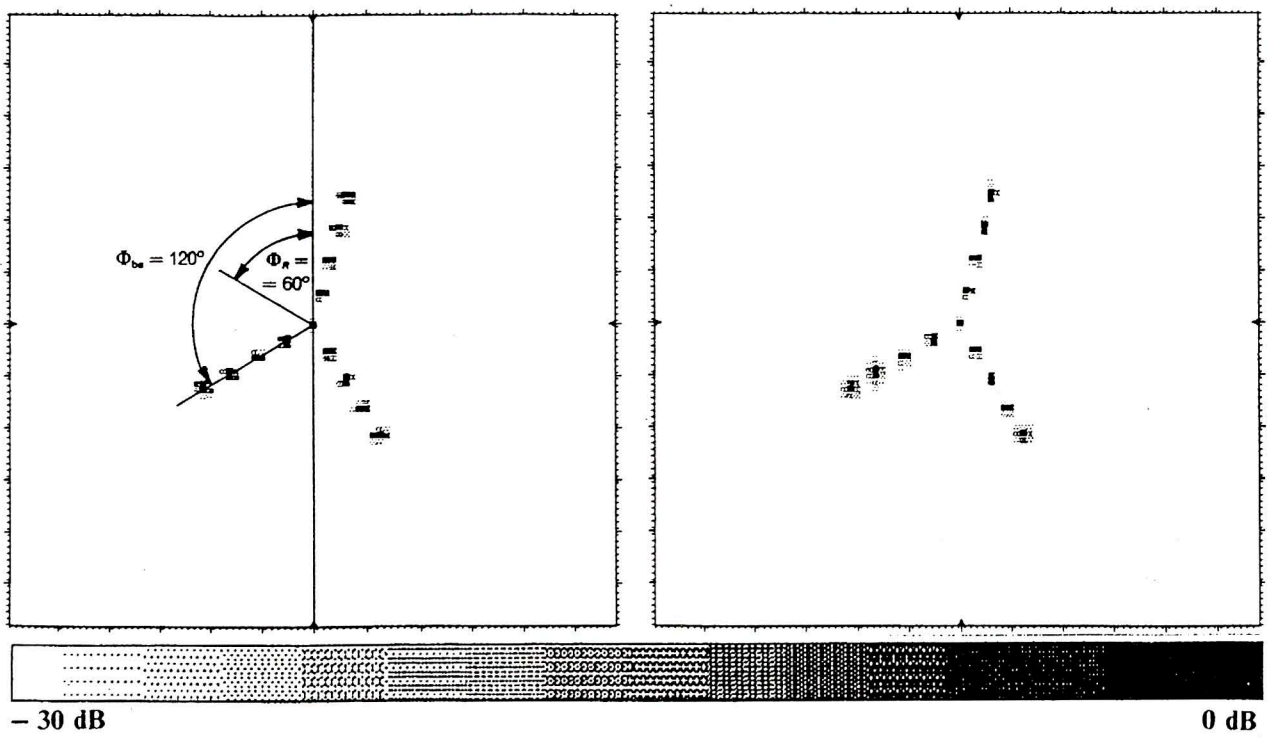

Fig. 8 - Simulated point scatterers (bistatic geometry) unfocused (1) focused (r)
$\delta R = 30cm$, $\lambda/\Delta\varphi = 30cm$, $\lambda = 2cm$, $\Theta_T = \Theta_R = 0^0$, $\Theta_R = 60^0$.

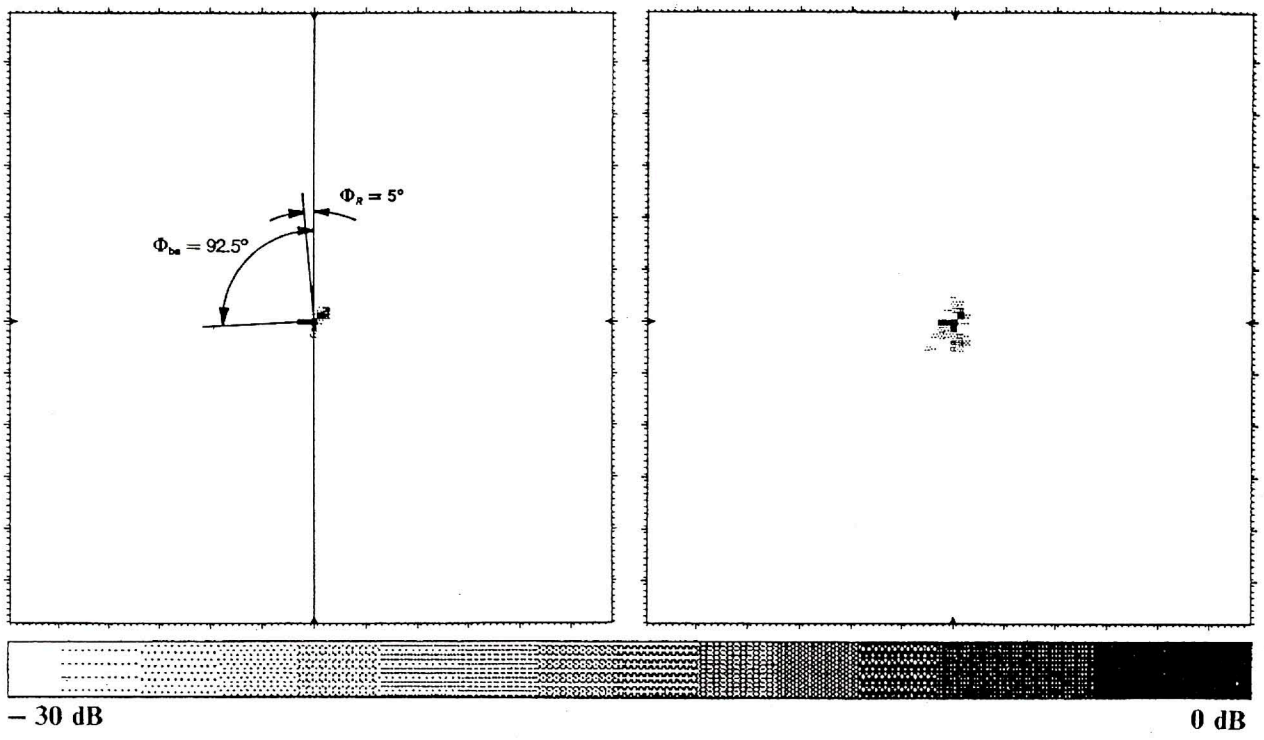

Fig. 9 - Simulated point scatterers (bistatic geometry) unfocused (1) focused (r)
$\delta R = 30cm$, $\lambda/\Delta\varphi = 30cm$, $\lambda = 2cm$, $\Theta_T = \Theta_R = 0^0$, $\Theta_R = 5^0$.

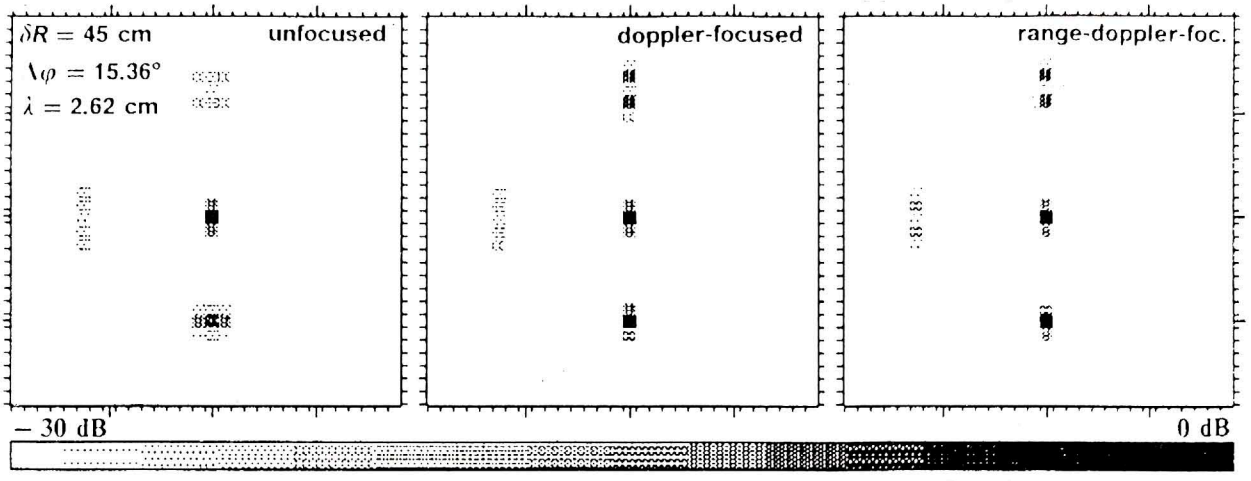

Fig. 10 - Monostatic simulation of point scatterers $\varphi_0 = 90^0$, $\Theta_0 = 0^0$

distance r from the axis of rotation an the angle interval $\Delta\varphi$ of data analysis. In this experiment the size of the targets was limited to a diameter of appromimately 3 meters. Therefore, the angle interval $\Delta\varphi$ must be chosen larger than in the simulations of chapter 3; these simulations have been calculated with $\Delta\varphi = 3.84^0$ and $f_0 = 15GHz$. Because of the smaller size of the target and a reduced sampling rate of the received signal, the frequency was set to $f_0 = 11.43GHz$ and the angle interval $\Delta\varphi = 15.36^0$ in order to demonstrate the defocusing effects. The results of the measurements are compared with simulations in figs. 10 and 13. In figs. 11 and 14 the unfocused point above thhe central point seems to be a double one; this effect is an artifact due to shadowing of this reflector by the others which are located in the lower part of the image.

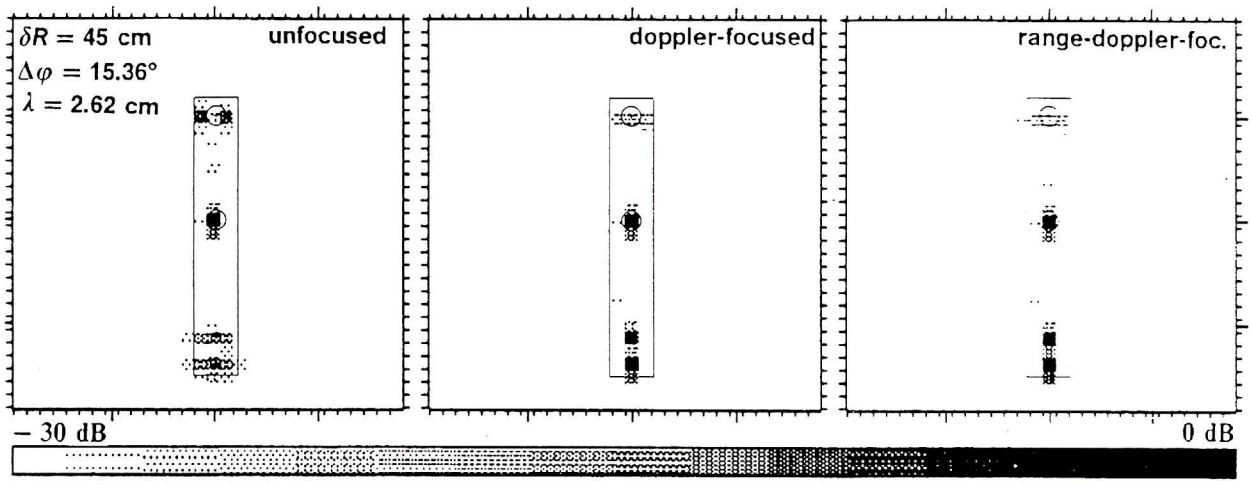

Fig. 11 - Monostatic measurement of biconical reflectors $\varphi_0 = 270^0$, $\Theta_0 = 0^0$.

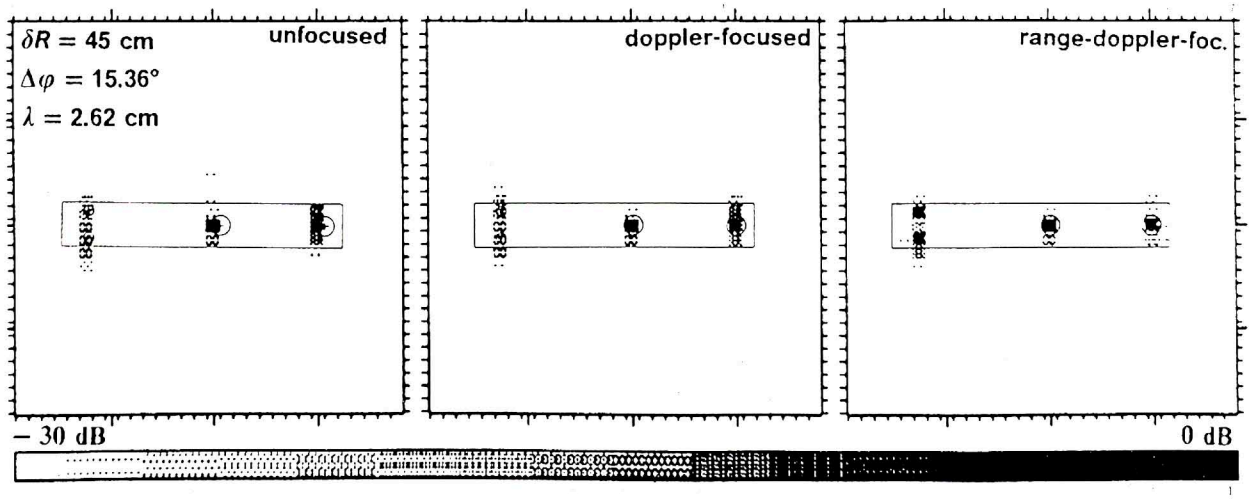

Fig. 12 - Monostatic measurement of biconical reflectors $\varphi_0 = 0^0$, $\Theta_0 = 0^0$.

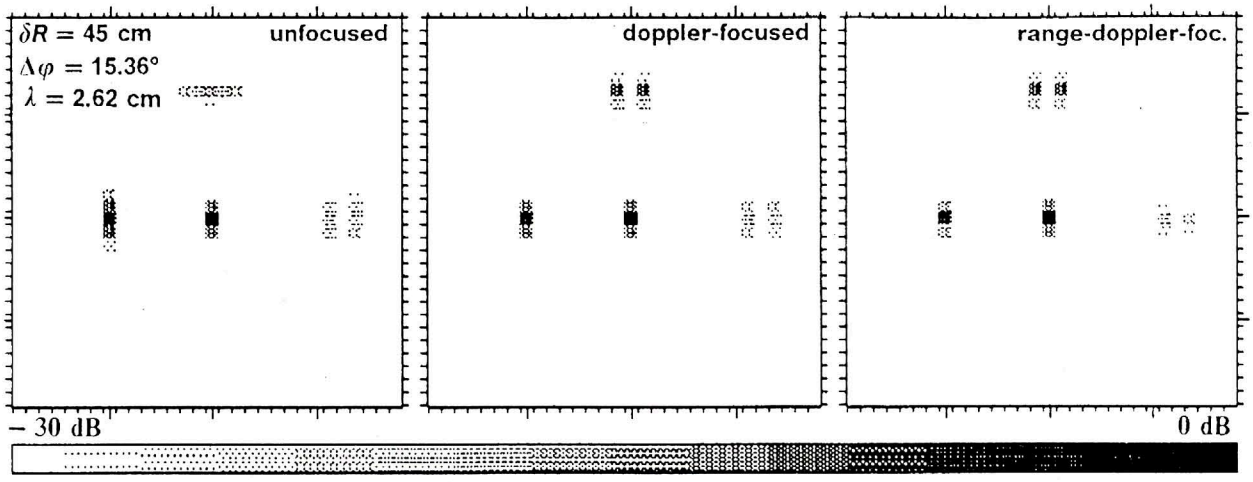

Fig. 13 - Monostatic measurement of biconical reflectors $\varphi_0 = 180^0$, $\Theta_0 = 0^0$.

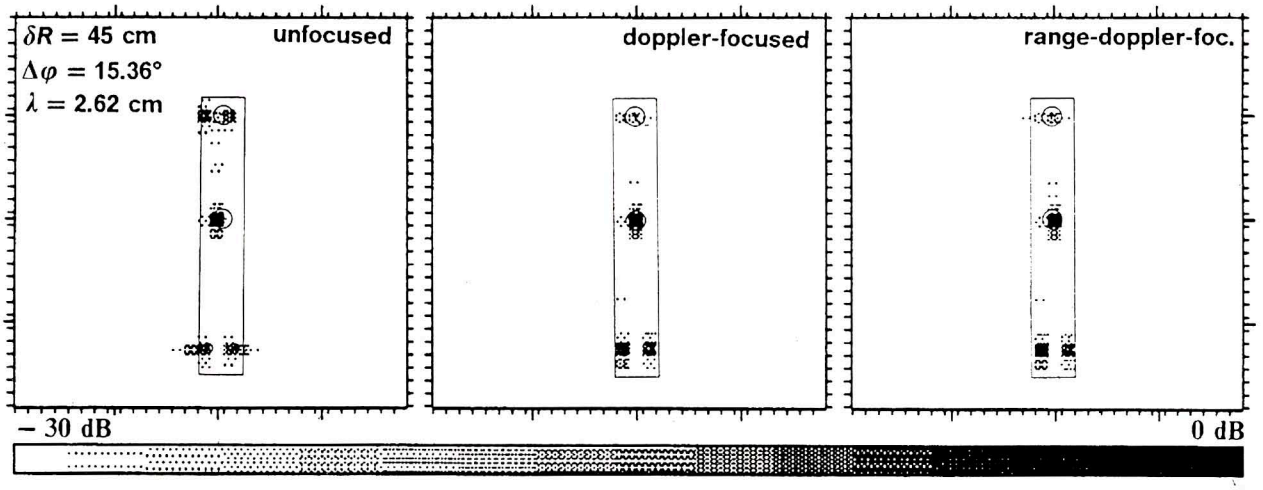

Fig. 14 - Monostatic measurement of biconical reflectors $\varphi_0 = 270^0$, $\Theta_0 = 0^0$.

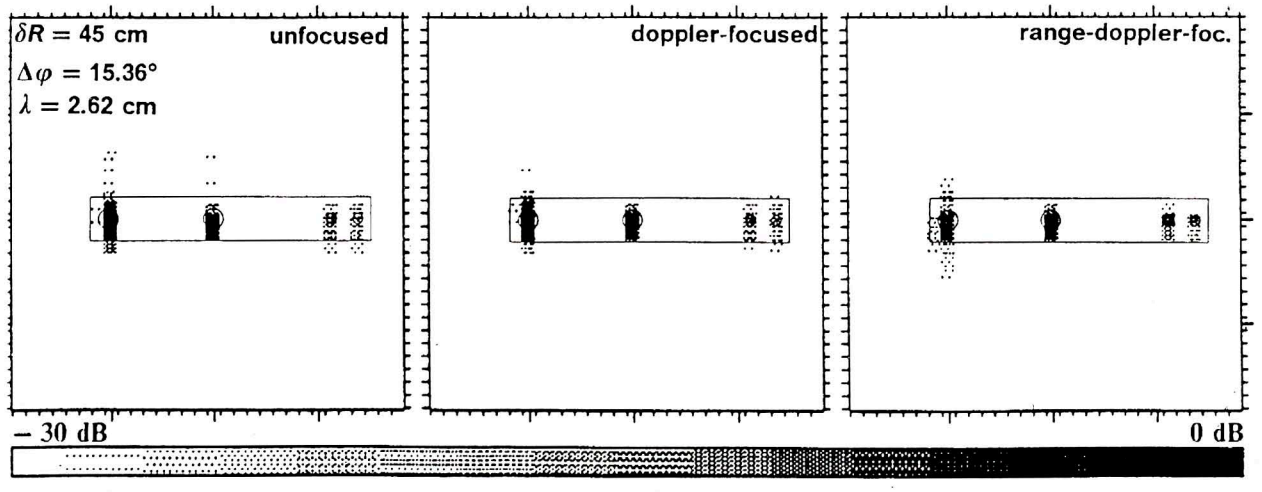

Fig. 15 - Monostatic measurement of biconical reflectors $\varphi_0 = 180^0$, $\Theta_0 = 0^0$.

3.2 The pheomenon of migrating glint points

The question to be answered is, whether the properties of imaging can always described by those of point scatterers. Scattering centers which are isotropically visible within the angle interval of data processing may fulfill this modell. Such has been showed in the upper chapters. But there exists an example, which can be solved by means of physical optics, even by means of geometrical optics (ray tracing), which does not fit the model of scattering points moving according the mechanical movement of rotation. We assume a right cylinder with an ellipsoid cross section rotating around its main axis. The left part of fig. 16 shows the mechanism of migrating glint points: If the broad side of the cylinder stands perpendicular to the monostatic incident ray (see the solid line of an ellipse), the line of glint will be seen in the middle.

A quarter turn lets migrate the glint point along cross range, untile a point of reversal is reached (see dashed line of an ellipse); the reflection from the narrow side will have its glint point in the middle again (seen dash-dotted line of an ellipse). The right part of fig. 16 shows the locus of glint point dependent on the angle of rotation φ. It may be deduced, that this locus has a period of 180°: the locus of

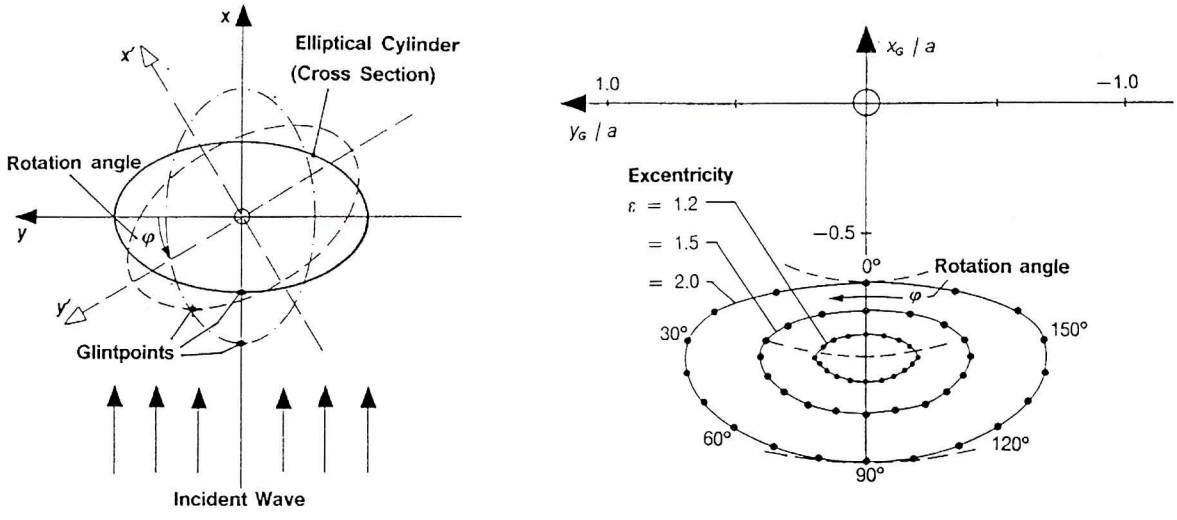

Fig. 16 - Migrating glint points (I) Elliptical Cylinder (r) Locus of Glint Point.

glint point during a whole turn of the elliptic cylinder will be passed twice - so it is edivent, that mechanical motion and locus of high do not conform. A further fact is given in fig. 16: the motion of a rotating surface point is going around the axis of rotation in a constant distance. The distance of the glint point (of the elliptic cylinder) and the axis of rotation changes between the great semi-axis and the small semi-axis of the ellipse.
The glint point is always located between the axis of rotatio n and the radar sensor.

A physical interpretation of this phenomenon is that glint points come up and disappear again with a small variation of the rotation angle. The behavior of such scattering points is a pronounced anisotropic one. The effective interval $\Delta\varphi$ of data analysis will be shortened with the effect of a strong non-optimal (cross range) resolution.
Fig. 17 shows, for two examples of ellipsoid cylinders, the succession of simulated glint points (with a constant amplitude): the upper example shows the complete locus of glint point in some steps for a small elliptic cylinder, the lower example only the left half of a greater one. In the left part ("unfoc.") the points are processed without focusing. The doppler variation at the lower point is similar to that of scattering point rotating around the axis of rotation; the upper point of the locus seems to move more rapidly in the opposite direction. The middle part of fig. 17 ("r-d-foc." = range-doppler-focused) shows the same scenario processed by means of the usual focusing algorithm; in the lower point the focusing is effective because doppler variations are in the same order and the same sense as the model of rotating scatterers. The point which is closer to the axis of rotation is defocused very violently. The reason is that doppler variation with the opposite sign is expected by the algorithm. The right part ("optimally-foc.") finally shows the points focused with an optimal algorithm. The locus of glint point can be estimated by a mathematical model and may be taken into account for focusing. This model is fulfilling the correspondence of down range variation and doppler shift (or cross range) versus rotation angle (more details see (Kleintz, 1992).

3.3 Monostatic measurements of an aircraft model

The phenomenon mentioned above is to be observed within the measurements at an aircraft model (Boeing 707, scale 1:13). This model is built up with carbon fibrous material and is simplified in its shape (i.e. without engines, windows, landing gear, etc.). Its fuselage consists of two ellipsoidal parts with the following dimensions: Vertical semiaxis a=15.8 cm, horizontal semiaxis b=12.9 cm, semiaxis of the forward part $c_1 = 103.2cm$ and semiaxis of the rear part $c_2 = 212.9cm$ (--> total lenght $\approx 316cm$). The wingspread is 300 cm; the wings are inclined 5° against the horizontal plane and twisted about 1° over the whole lenght; this effect produces a migration of glint points,

dependent on the aspect angle. Widespread areas of reflection, e.g. the edge of wings or the broadside of fuselage, with nonconstant curvature will be defocused because of the effect of migrating glint points. Whereas point equivalent scatterers, such like the nose of an aircraft or the tips of wings, are focused quite well.

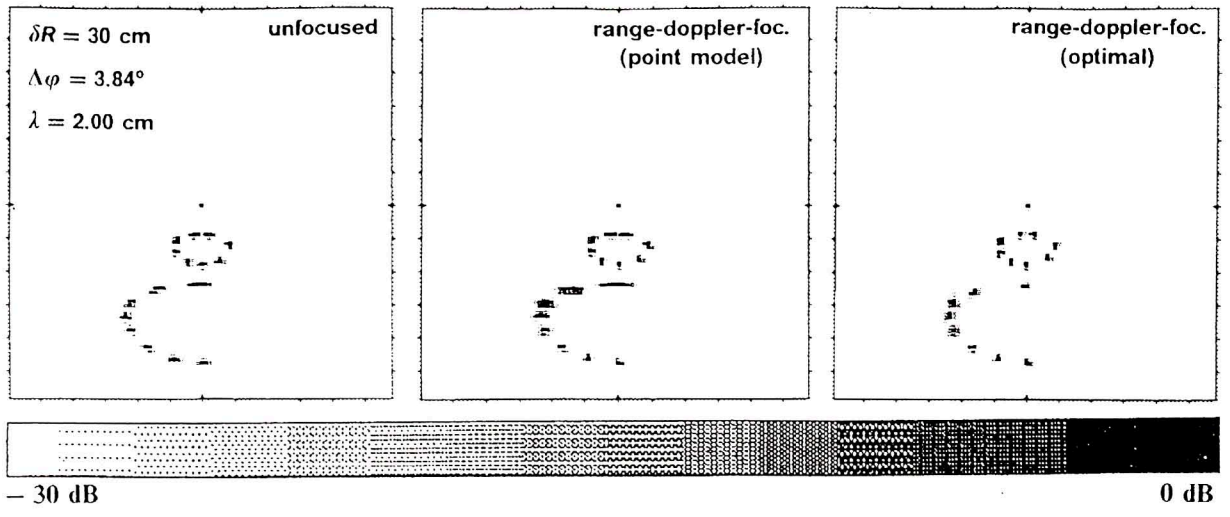

Fig. 17 - Locus of glint point (simulation).

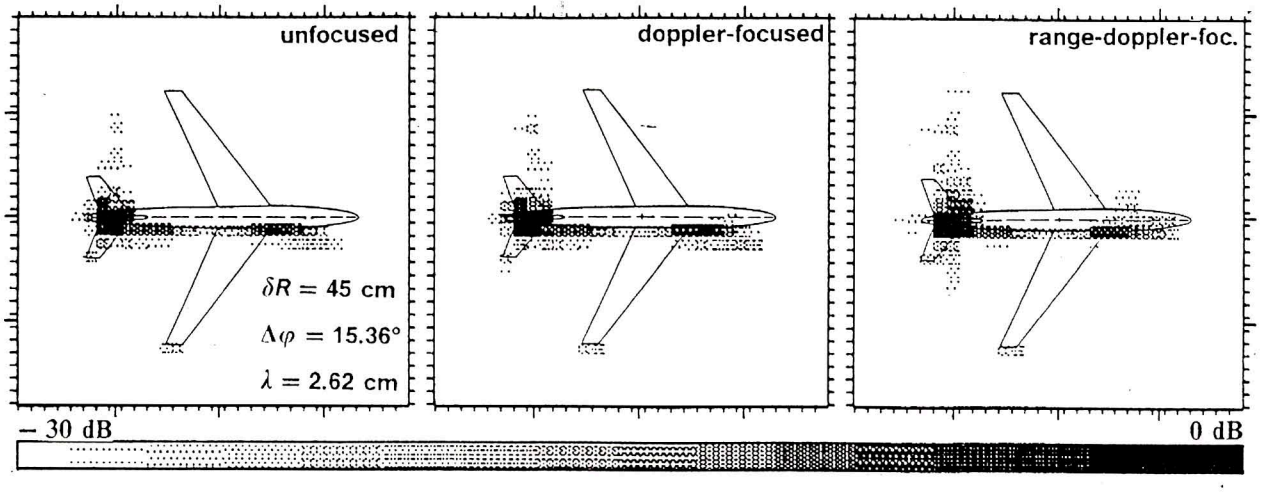

Fig. 18 - Measurement of an aircraft model $\varphi_0 = 80.00^0$, $\Theta_0 = 0^0$.

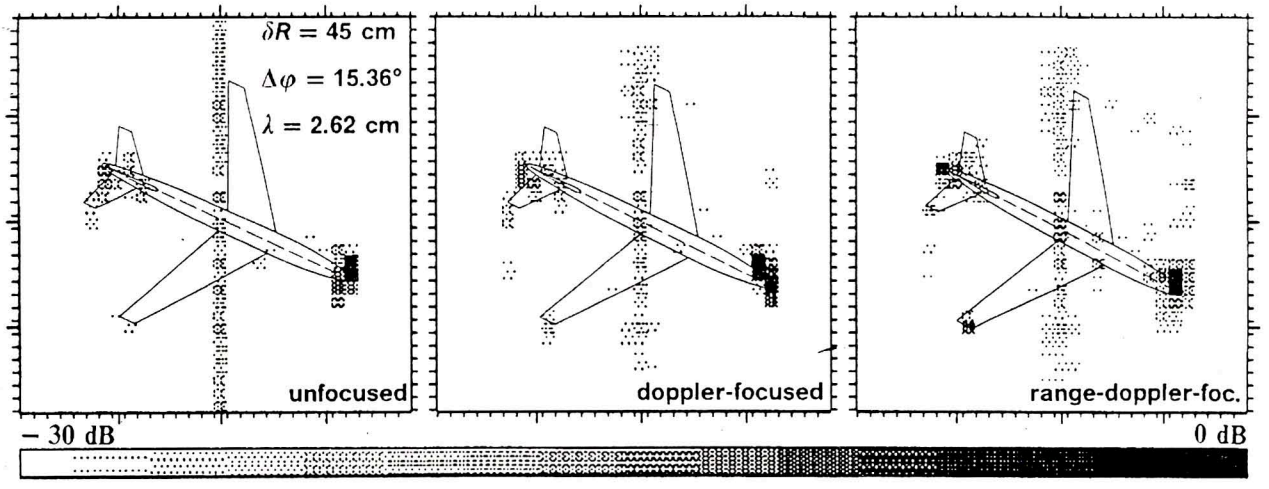

Fig. 19 - Measurement of an aircraft model $\varphi_0 = 105.68^0$, $\Theta_0 = 0^0$.

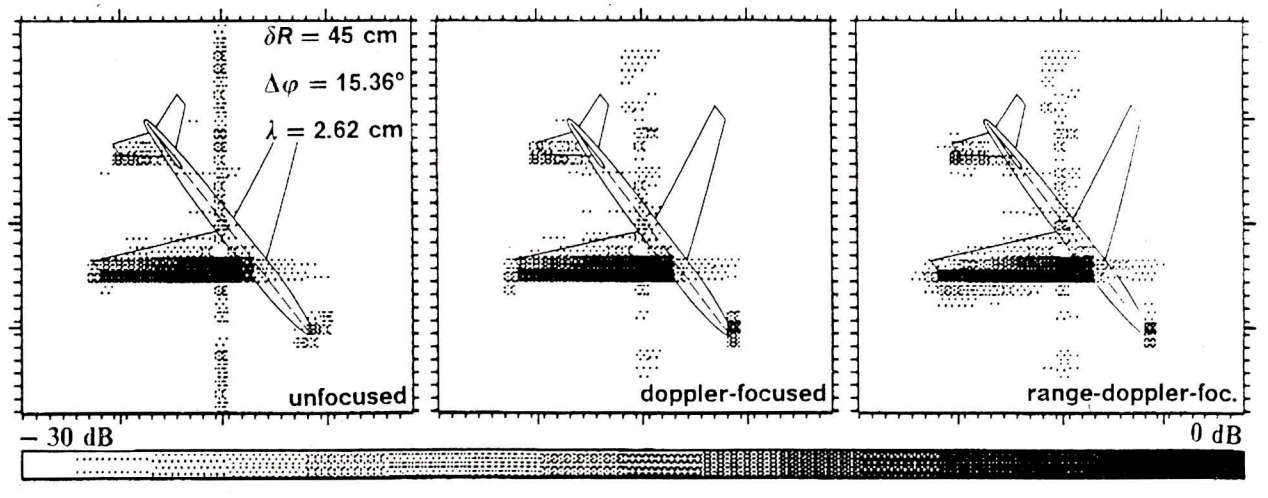

Fig. 20 - Measurement of an aircraft model $\varphi_0 = 131.36^0$, $\Theta_0 = 0^0$.

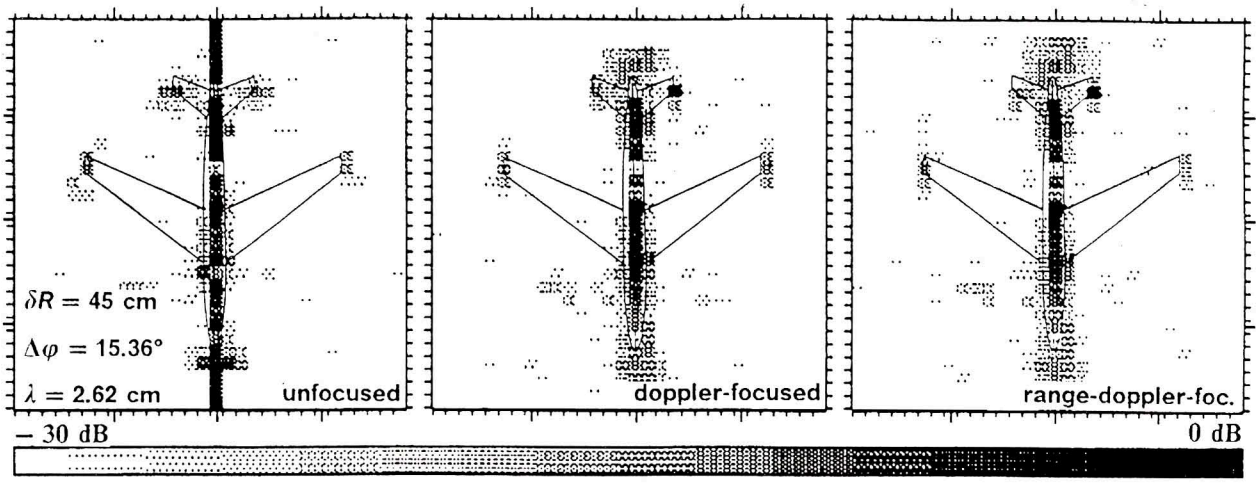

Fig. 21 - Measurement of an aircraft model $\varphi_0 = 170.00^0$, $\Theta_0 = 0^0$+.

CONCLUSION

The basis of radar imaging is the coordination of geometry and radar echo signals.

For this, the quantities range and doppler shift may be related for bistatic geometry as well as for monostatic measurements by a linear far-field transform to the cartesian coordinates x and y of the radar target. The scattering model of the target, assumed to be composed of a great number of scattering points located on its surface, has been validated by mono- and bistatic simulation and by monostatic measurements. The latter have been taken from biconical reflectors in order to validate the theory of point imaging, and from an aircraft model (i.e. a "real" target); the behavior for a "real" target does not generally fit the point scatterer model. Its boundaries are pointed out theoretically about the properties of migrating glint points at an elliptical cylinder: it is shown by simulation that nevertheless by a-priori-information about the locus of glint points optimal focusing is possible. The effects of migrating glint points can also be observed within the measurements at the aircraft model, e.g. at surfaces with nonconstant curvature (wing edges, fuselate etc.).

REFERENCES

Graf G., *Doppler frequenzanalyse rotierender Körper* Dissertation TU-München 1972.

Kleintz M., *Ein Auswertesystem zur 2-dimensionalen Abbildung rotierender Objekte* DFVLR IB-87/5.

Kleintz M., Rekonstruktion 2-dimensionaler Rückstreu-Signaturen eines rotierenden Objekts Vortrag beim Symposium Radartechnik der DGON, Bremen November 1986.

Kleintz M., *Beiträge zur zweidimensionalen Abbildung rotierender Objekte* Vortrag beim Symposium Radartechnik der DGON, Ulm Oktober 1989.

Kleintz M., *Zur fokussierten zweidimensionalen Abbildung aus monostatischen und bistatischen Range-Doppler-Messungen mit einem Kohärenten Kurzpulsradar mit fest eingestellten Range-Gates im Zentimeter-Wellenbereich* DLR-Forschungsbericht (to be published in 1992).

Kleintz M., *Monostatische Meβbeispiele* zur fokussierten zweidimensionalen Range-Doppler-Abbildung im Zentimeter-Wellenbereich Unpublished paper, October 1991.

Bethke K.H., *Ein schnelles zweidimensionales Radarabbildungsverfahren für rotierende Objekte und eine Analyse der Abbildungsqualität* DFVLR FB-88/51.

Bethke K.H., *Untersuchungen zue Störstreuung un Methoden zu deren Unterdrückung bei bodennahen Radarrückstrahlmessungen* DFVLR FB-85/42.

Marko H., *Die Systemtheorie homogener Schichten* AEÜ S. 327-333 1967.

Chaloupka H., *Systemtheoretische Betrachtung elektromagnetischer Abbildungsverfahren* Kleinheubacher Berichte Band Nr. 28 1985.

Mensa D.L., *High Resolution Radar Imaging* Artech House Inc, Washington 1981.

Papoulis A., *The Fourier Integral and its Application* McGraw-Hill, New York 1962.

Brigham E.O., *The Fast Fourier Transform* Englewood Cliffs, N.Y.: Prentice Hall 1974.

Hamming R.W., *Digital Filters* Englewood Cliffs, N.Y.: Prentice Hall 1977.

Ruck G.T. et al. *Radar Cross Section Handbook* Plenum Press, New York / London, 1970.

Gröbner W. und Hofreiter N., *Integraltafel (Teil I und II)* Springer-Verlag, Wien, Innsbruck 1958.